

Integrated seismic and electromagnetic model building applied to improve subbasalt depth imaging in the Faroe-Shetland Basin

Martin Panzner¹, Jan Petter Morten², Wiktor Waldemar Weibull³, and Børge Arntsen⁴

ABSTRACT

Subbasalt imaging has gained significant interest in the last two decades, driven by the urge to better understand the geologic structures beneath volcanic layers, which can be up to several kilometers thick. This understanding is crucial for the development and risking of hydrocarbon play models in these areas. However, imaging based on the reflection seismic data alone suffers from severe amplitude transmission losses and interbed multiples in the volcanic sequence, as well as from poor definition of the subbasalt velocity structure. We have considered a sequential imaging workflow, in which the resistivity model from joint controlled-source electromagnetic and magnetotelluric data

inversion was used to update the velocity model and to improve the structural definition in the migrated seismic image. The quantitative link between resistivity and velocity was derived from well data. The workflow used standard procedures for seismic velocity analysis, electromagnetic data inversion, and well analysis, and thereby allowed detail control and input based on additional geophysical knowledge and experience in each domain. Using real data sets from the Faroe-Shetland Basin, we can demonstrate that the integration of seismic and electromagnetic data significantly improved the imaging of geologic structures covered by up to several-kilometer-thick extended volcanic sequences. The improved results might alter the interpretation compared with the imaging results from seismic data alone.

INTRODUCTION

Subbasalt imaging using reflection seismic data is challenging for several reasons. First, it is difficult to identify continuous reflection events below the top basalt reflector. Basalts can have very high acoustic impedances and are usually interlaid with much softer material, such as volcanoclastics and other types of sediments. Such a sequence of high-acoustic-impedance contrasts causes serious transmission losses and leads to the development of internal multiples. Interference of these multiples, which have a small time delay, leads to an effective shift in the frequency spectra toward the low frequencies (O'Doherty and Anstey, 1971). Subbasalt reflection events are therefore low frequent, small in amplitude, and may be below the noise level or diluted by the strong interbed multiples that develop within the basalt sequence.

Another major challenge is the definition of the velocity model, which is needed for successful depth migration. The main lithologies that must be represented are as follows: shallow low-velocity sediments, a high-velocity basalt sequence beneath, eventually some low-velocity subbasalt sediments, and a high-velocity basement (Figure 1). Detecting and quantifying the low-velocity subbasalt sediment layer are still unsolved challenges. Due to the weak and often discontinuous subbasalt reflectors, it is difficult to define structural boundaries, such as the base of the basalt sequence or the top of the basement. Further, the basalt sequence has significantly higher velocities than the sediments below, that leads to small reflection angles for the subbasalt events (dashed blue lines in Figure 1). Conventional moveout-based velocity analysis may therefore give poor results. We will elaborate on that in the section "Seismic data velocity analysis."

Manuscript received by the Editor 2 March 2015; revised manuscript received 16 September 2015; published online 29 January 2016.

¹Norwegian University of Science and Technology, Institute of Petroleum Technology and Applied Geophysics, Trondheim, Norway and Electromagnetic Geoservices ASA, Trondheim, Norway. E-mail: martin.panzner@ntnu.no; mp@emgs.com.

²EMGS ASA, Trondheim, Norway. E-mail: jpmorten@emgs.com.

³University of Stavanger, Department of Petroleum Engineering, Stavanger, Norway. E-mail: wiktor.w.weibull@uis.no.

⁴Norwegian University of Science and Technology, Institute of Petroleum Technology and Applied Geophysics, Trondheim, Norway. E-mail: borge.arntsen@ntnu.no.

© 2016 Society of Exploration Geophysicists. All rights reserved.

Different strategies have been suggested to overcome the above-mentioned challenges for velocity model building. Typically, these approaches incorporate additional information either from enhanced seismic data acquisition and processing or from other geophysical survey techniques, such as potential field methods, controlled-source electromagnetics (CSEM), and magnetotellurics (MT).

Fruehn et al. (2001) and White et al. (2003) use long-offset first arrivals for traveltimes tomography, attempting to determine the basalt and subbasalt velocity structure. First arrivals from refracted waves in the high-velocity basalt sequence can often be accurately picked, and the bulk velocity of the basalt sequence can be recovered using these data (solid green lines in Figure 1). Sometimes, traveltimes of refracted waves propagating in the basement can also be picked (dashed green lines in Figure 1), which helps to determine the basement velocities. However, the velocities of the subbasalt sediments are poorly constrained by these basement refractions because the velocity and the thickness of this low-velocity zone (LVZ) are unknown (e.g., Funck et al., 2008). There are no first arrivals from refracted waves propagating in the LVZ that would allow direct velocity estimation. Fruehn et al. (2001) overcome this limitation by using the velocities for the subbasalt sequence found by conventional velocity analysis beyond the feather edge of the basalt flows.

Gallagher and Dromgoole (2007) achieve some subbasalt imaging improvements by optimizing acquisition and processing for low-frequency reflection seismic data, and thereby they reduce the impact of high-frequency noise in the data. These authors also manage to improve the moveout-based velocity analysis by taking a geologic a priori model into account. However, these approaches to improve the velocity model were not successful for the data set considered in this paper.

Potential field methods such as gravity and gravity gradiometry can delineate the lateral extent of a density anomaly. However, such information does not help to overcome the imaging difficulties addressed in this paper. The geology of an extended basalt sequence can to some extent be considered as a 1D layered earth. In this case,

gravity data by themselves do not resolve the thickness unless the mass density contrast for this anomalous basalt layer and the layers below are precisely known (e.g., Oldenburg, 1974).

Marine EM methods use another physical property of volcanic rocks: They are very resistive in contrast to sediments. This fact makes EM methods well suited for imaging the basalt sequence and the transition to the more conductive subbasalt sediments. In this paper, we consider marine MT and the CSEM method. Marine MT source signals are part of the earth's natural EM spectrum in the frequency range of 0.001–1 Hz (e.g., Chave and Jones, 2012). For the marine CSEM method, an alternating electric field in the frequency range 0.1–10 Hz is emitted from a horizontal electric dipole, which is towed behind a vessel (e.g., Eidesmo et al., 2002). The CSEM and MT signals are recorded by receiver stations on the seafloor.

The amplitude and the phase of the EM fields, acquired over a range of frequencies, contain direct information about the resistivity distribution in the subsurface. The EM amplitude is governed by the skin depth effect, which describes the attenuation of propagating EM signals according to resistivity and frequency. In a uniform medium, the skin depth is the distance over which amplitude is reduced by a factor $1/e$, and it is proportional to $\sqrt{R/f}$, where R is the resistivity and f is the frequency. Traveltime effects are captured by the phase, which is determined by the phase velocity. The phase velocity in a uniform medium is proportional to \sqrt{Rf} . Signals used for CSEM and MT have lower frequency content and longer wavelengths compared with the seismic source signal, and the fields are therefore not scattered in the same way by small-scale structures within the basalt. Moreover, the propagation governed by the Maxwell equations give rise to different propagation effects than seismic.

Low-frequency MT signals can penetrate deeply, and they have been successfully used to image large-scale resistivity variations in the earth's crust (e.g., Naif et al., 2013). Marine CSEM data have traditionally been used to map resistivity anomalies due to hydrocarbon accumulations or salt structures in the upper few kilometers of the subsurface (e.g., Eidesmo et al., 2002; Morten et al., 2013).

Colombo et al. (2008) managed to improve subsurface imaging by jointly inverting land seismic and MT data to derive the subbasalt velocity structure. Marine subbasalt imaging incorporating seismic traveltimes, gravity, and marine MT data is demonstrated by Jegen et al. (2009) and Heincke et al. (2014), using 1D and 3D joint inversion algorithms, respectively. The feasibility of using marine CSEM data for imaging of a basalt layer is suggested by MacGregor and Sinha (2000). Herredsvella et al. (2012) and Alumbaugh et al. (2013) confirm in synthetic modeling and inversion studies that a combination of CSEM and MT data can significantly increase the sensitivity to the subbasalt resistivity structure. It is also shown that the marine MT data alone typically do not have sufficiently high-frequency content to resolve the basalt layer due to the water column acting as a low-pass filter. High-frequency CSEM data are needed to reconstruct the basalt layer. Using a real data set, Hoversten et al. (2013) demonstrate that marine CSEM and

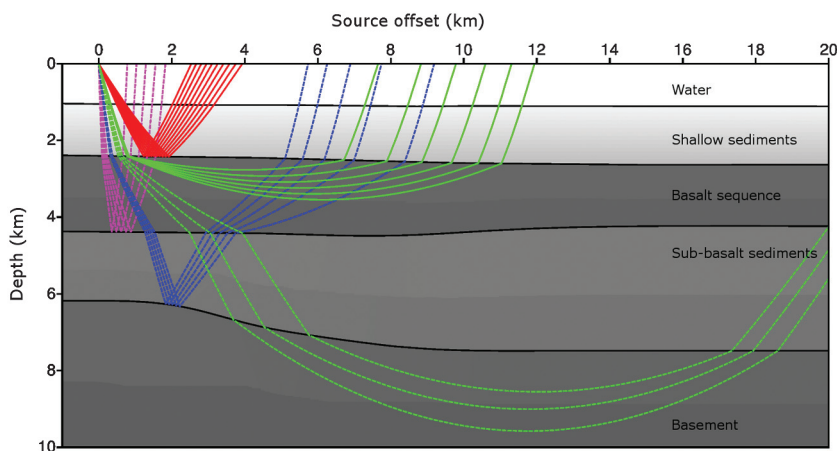


Figure 1. Ray-tracing through a velocity model containing a high-velocity basalt sequence. Raypaths for direct reflections are shown for the top basalt reflector (red), the base basalt reflector (magenta), and the top basement reflector (blue), illustrating small reflection angles for subbasalt reflection events. Traveltimes from refracted events in the basalt sequence and the basement (green) can be used for first arrival traveltimes tomography.

MT data in combination can image the thickness and the extent of a basalt layer, as well as the sediment and basement structures underneath.

The previous studies primarily focus on improving the parameter models for the subsurface resistivity and velocity distribution. In this paper, we describe a workflow for integrating EM data for seismic velocity model building and demonstrate that the updated velocity model will improve the seismic depth imaging results. The structural information and the quantitative resistivity distribution, recovered by the EM methods, can be used to enhance the velocity model (Panzner et al., 2014). The final interpretation of the data will benefit not only from the improved depth imaging due to the more realistic velocity model, but also from the resistivity distribution, which can be covisualized with the migrated seismic image. We consider real data from a regional seismic 2D survey and two EM surveys acquired in the Faroe-Shetland Basin.

The paper is organized as follows: First, we outline the methodology for integrated seismic and EM model building, and describe the theoretical motivations. We then demonstrate the workflow on real data and describe the seismic velocity analysis and the EM resistivity inversion. Next, we establish a relationship between velocity and resistivity based on well data and use that to update the velocity model. Finally, we present and discuss the improved imaging results.

MOTIVATION AND WORKFLOW

Imaging results achieved through multiparameter estimation can leverage the complementary information from several geophysical measurements. To this end, many authors describe procedures based on different kinds of joint inversion software to image the subsurface (e.g., Colombo and De Stefano, 2007; Gallardo and Meju, 2007; Moorkamp et al., 2011; Medina et al., 2012). In order for a joint inversion approach to be successful, the software must be able to couple the model parameters to which the different data types are sensitive. Parameter coupling using structural similarity constraints is described by Gallardo and Meju (2007). Another alternative is to impose empirical parameter relations (e.g., Jegen et al., 2009) or even both of these types of constraints (e.g., Moorkamp et al., 2011). These numerically defined couplings are usually rigid during the course of the iterative joint inversion. Imaging artifacts can arise if, e.g., the different data types mostly give information about non-overlapping parameter regions or if there are structural boundaries that are only present in one parameter type. For instance, the differences in sensitivity to the subbasalt properties between seismic and EM data are a complication for joint-inversion approaches. Reflection seismic data can provide detailed structural and velocity information for the shallow subsurface above the basalt sequence, but they fail to determine the velocity structure beneath. On the other hand, EM methods can only provide large-scale representation of the structure, but for the entire subsurface of interest. Therefore, we focus on sequential inversion and imaging. This approach is conceptually simpler than a joint inversion, and it allows flexibility in construction of the

parameter couplings and constraints. The type and strategy for coupling the model parameters can vary during the course of the sequential inversion and imaging procedure.

Our workflow for integrating seismic and EM data for velocity model building extends established depth imaging methodologies (Figure 2). As a first step, we consider seismic velocity analysis and depth imaging, which result in a preliminary velocity model and seismic image. From these results, it is possible to extract some structure. In particular, the top basalt surface, as well as the velocity structure for the shallow sediments, can be found. The top basalt horizon is then used as a constraint in a subsequent EM data inversion, resulting in a resistivity model that partially conforms to the seismic interpretation. We establish a parameter relation between velocity and resistivity based on well data, which allows us to update the uncertain subbasalt velocity model using predictions from the resistivity model. The resistivity model is achieved on a coarser

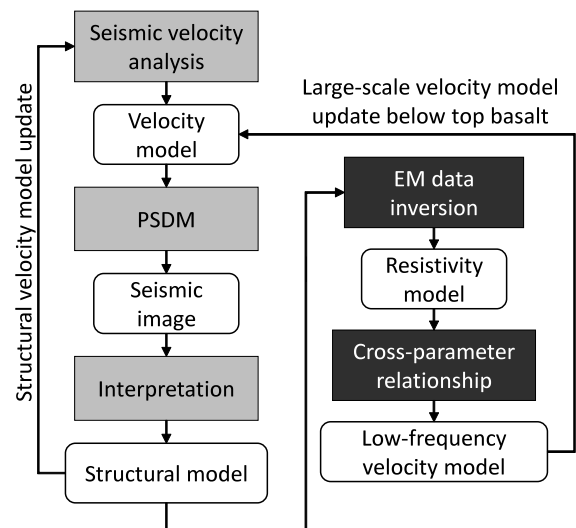


Figure 2. Workflow for integrated seismic and EM data imaging.

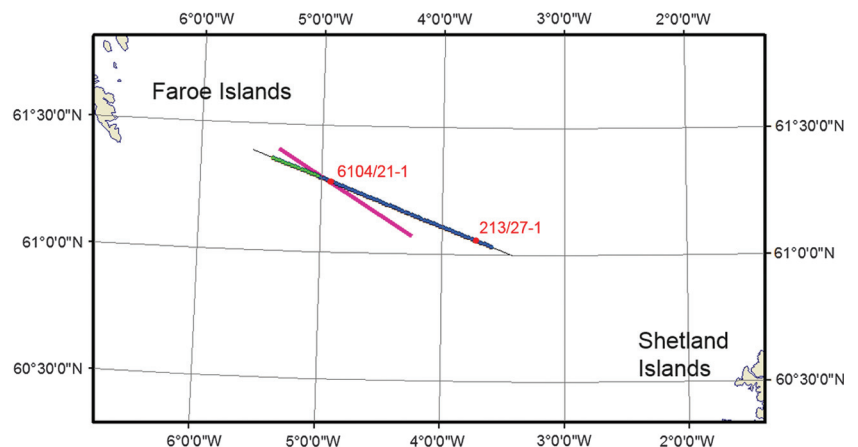


Figure 3. Map showing the location of the FLA_06 seismic line (magenta line), the location of the CSEM and MT receivers used for this study, from the 2012 survey (blue dots), from the 2014 survey (green dots), and the CSEM tow line (thin black line). The locations of the Brugdan well (6104/21-1) and the Rosebank well (213/27-1) are also shown (red dots).

scale than what is resolved by the seismic data (due to the different frequency content and propagation physics), but the velocity model obtained from the EM data inversion can still be used for seismic depth imaging on smaller length scales. This is because only the traveltimes need to be accurately represented to image the structure, and correct traveltimes can be predicted even with a smooth velocity model. In this way, the velocity model is updated with low-frequency information to complement the interpreted structural information. The updated velocity model can be used for another iteration of seismic velocity analysis and depth imaging benefiting from the improved subsalt velocity structure. Related workflows are studied by, e.g., Colombo et al. (2014) and Um et al. (2014) in the context of subsalt imaging. We emphasize that couplings between the velocity and resistivity models involved in the workflow can be based on interpreted structure from depth imaging results and quantitative predictions from empirical cross-parameter relationships. In our approach, the parameter couplings and the flow of information between the two data domains (seismic and EM) are manually controlled and can be modified in each step, reflecting geology-specific knowledge and experience. We believe this to be a strength of the workflow, allowing us to benefit from established best practices and understanding of the underlying geophysics. The seismic velocity analysis and EM inversion are performed with

standard software tools that were not specifically designed for integrated processing workflows.

SUBSURFACE MODEL BUILDING

We will consider data from a regional 2D seismic line, as well as subsets of data from two separate EM surveys; the survey layouts are shown in Figure 3. The seismic line has an angle of 10° to the CSEM and MT line, and both survey lines cross at approximately the Brugdan well (6104/21-1) location.

The data were acquired in the Faroe-Shetland Basin. The development of this basin was strongly influenced by the breakup of the North Atlantic, followed by extensive magmatism in the Paleocene and Eocene ages. Extrusive igneous rocks dominate the northwest margin of the basin. The volcanic complex is a succession of volcanoclastics at the base, a mix of volcanoclastics and flow basalts in the middle, and thick flows at the top. The thickness of the volcanic sequence decreases toward the southeast (Gallagher and Dromgoole, 2007).

Seismic data processing and velocity analysis

The seismic 2D line is called FLA_06, and it was acquired over the East Faroe High as part of the Faroes Large Aperture Research Experiment (Fruehn et al., 1998). Long-offset data were obtained in a two-vessel operation, in which both vessels were equipped with a source and a 6000 m long streamer. Both vessels were shooting alternately, while sailing at a constant separation along the same profile. Assuming reciprocity, the data were sorted and binned into supergathers with up to 18 km offset, 100 m receiver spacing, and 100 m shot spacing. For the depth imaging, we used reflection data with offsets up to 12 km. Prior to the velocity analysis and the depth imaging, the data set was processed using the following steps: source estimation and deconvolution, surface-related multiple attenuation (SRME), semblance analysis, multiple attenuation using the Radon transform, low-pass filter (30 Hz), as well as top mute and inner mute. A time stack of the processed data is shown in Figure 4. A major challenge with this data set is to tackle the different types of multiples in the data, i.e., seafloor multiples; secondary multiples from the top-basalt interface; and strong interbed

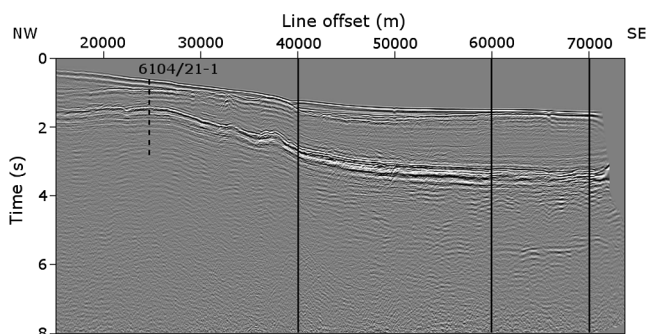
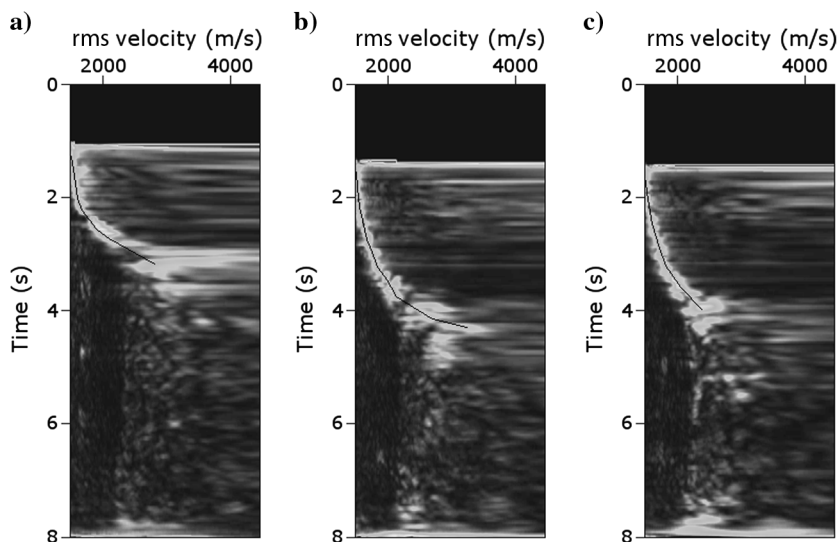


Figure 4. Time stack of the processed data. The location of the Brugdan well (6104/21-1) is indicated by the dashed black line. The solid black lines indicate the position of the semblance plots as shown in Figure 5.

Figure 5. Semblance plot for the CMP gathers at line offsets (a) 40, (b) 60, and (c) 70 km.



multiples that develop within the basalt sequence. SRME was successfully used to remove the seafloor-related multiples, and Radon-transform-based multiple attenuation techniques were used to attenuate the secondary multiples from the top-basalt interface. However, the intrabasalt multiples are difficult to eliminate due to the small velocity separation between the multiples and the primary reflections from within the basalt sequence.

The velocities of the suprabasalt sediments are well-defined by the reflection data and can be picked from semblance gathers down to the top-basalt reflector (Figure 5). Dix's equation was then used to convert the rms velocities into interval velocities.

Below the top basalt reflection, it was not possible to pick velocities on the semblance gathers. We extrapolated the sediment velocities linearly and depth migrated the seismic data using an acoustic 2D reverse time migration (RTM) (Weibull and Arntsen, 2013) to

locate the top-basalt reflector at depth. Subsurface angle common-image gathers (SA-CIGs) were computed to validate the suprabasalt velocity model. The angle gathers show flat reflectors down to the top of the basalt sequence (see also Figure 6c), which gives us confidence that the velocity model for the overburden above the basalt is valid.

To further improve the velocity model, we adopted a strategy from velocity model building in the presence of salt, called salt flooding. We "flooded" the velocity model below the top-basalt reflector with a constant basalt velocity. The basalt velocity was estimated to be 4900 m/s by analyzing the refracted waves from the basalt layer. The data were then migrated again, and subsurface angle gathers were recomputed. The angle gathers show some flat events with small reflection angles below the base of the basalt, but they also showed a number of curved events with residual move-

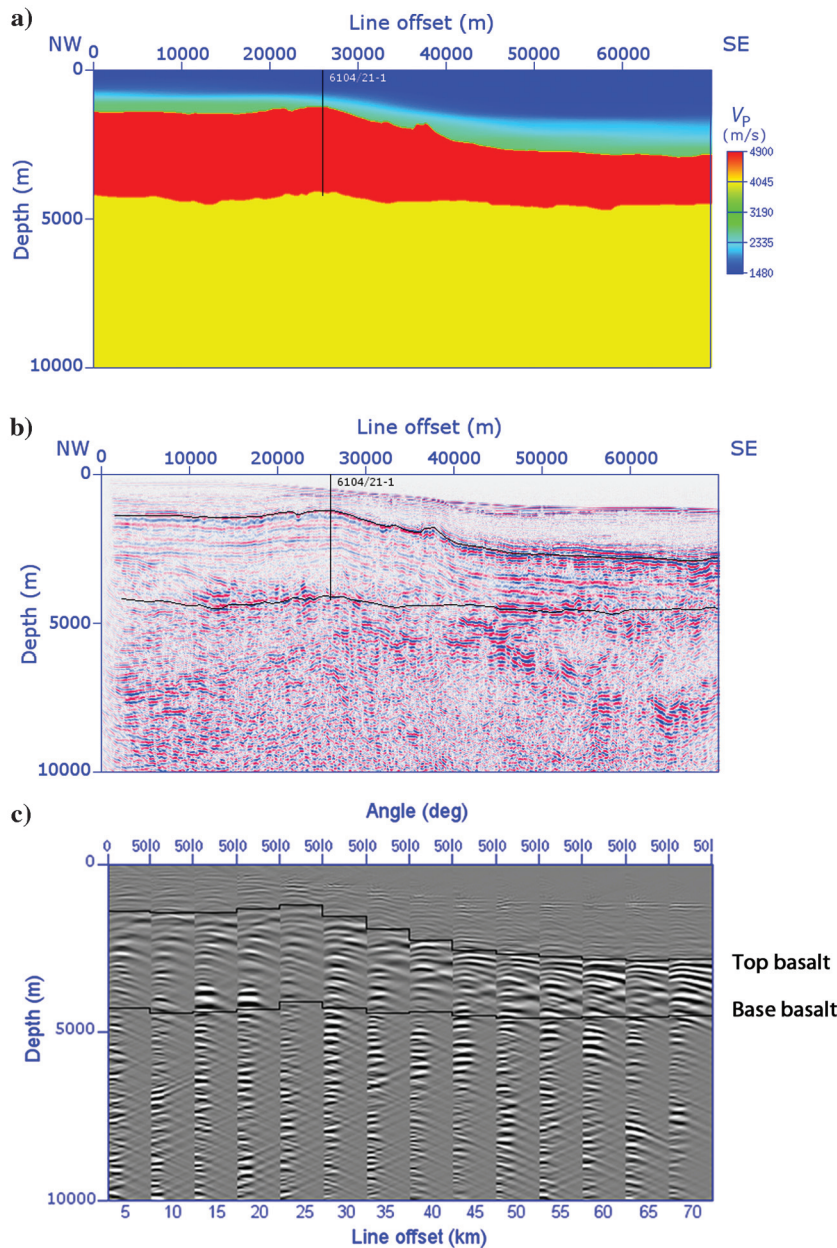


Figure 6. Display of the velocity model (a) based on seismic data only, (b) the corresponding depth-migrated seismic image, and (c) the subsurface angle common-image gathers for different positions along the line.

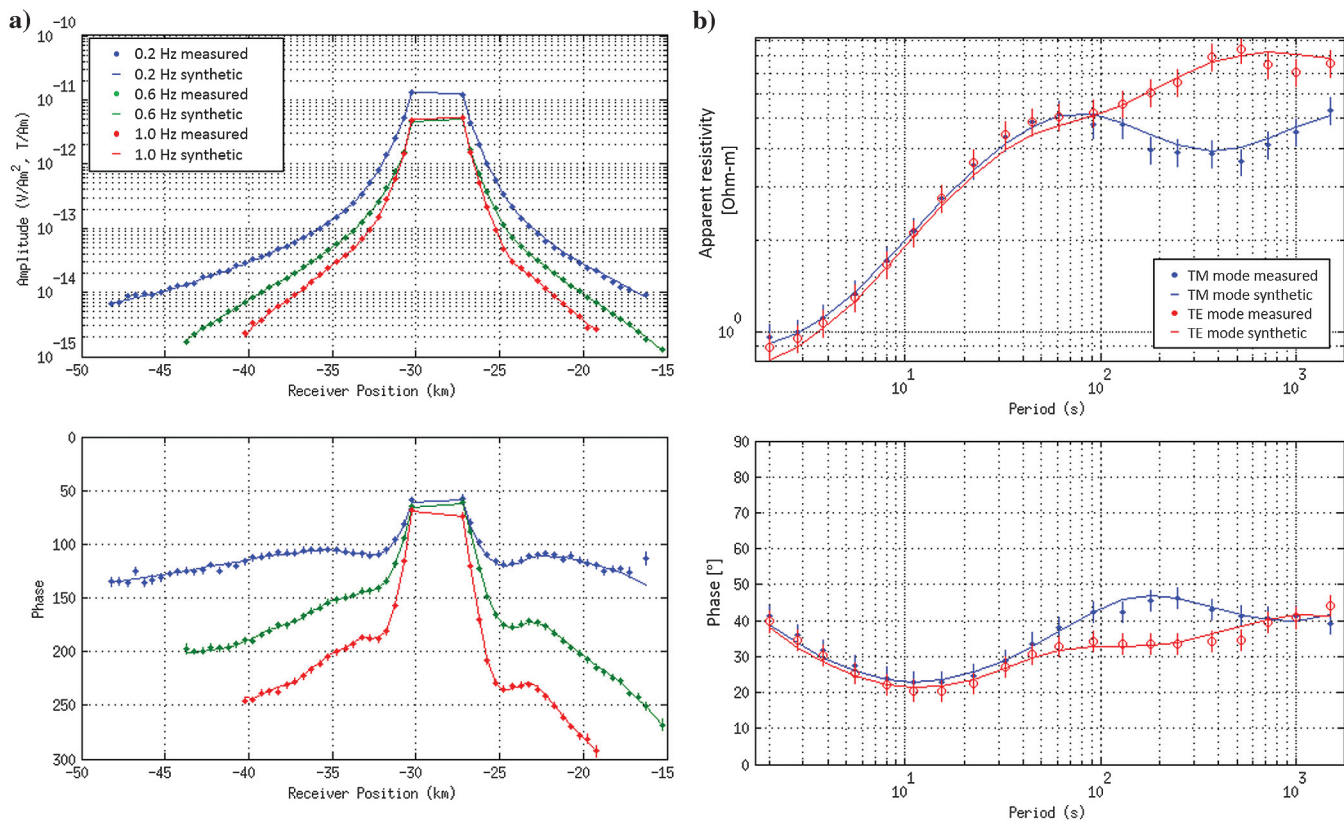
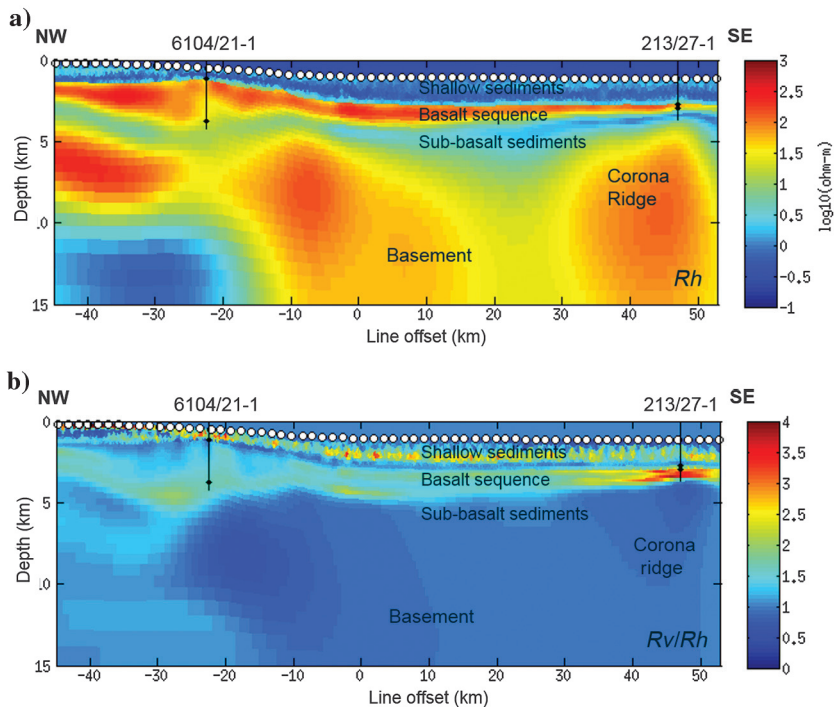


Figure 7. Display of measured data (dots) and synthetic data (straight line) from the inverted resistivity model. The (a) CSEM data and (b) MT data are shown for a receiver close to the Brugdan well location.

Figure 8. Model of the (a) horizontal resistivity and (b) electric anisotropy recovered from anisotropic CSEM and MT joint inversion. The resistivity scale is such that the resistive basalt and the deep basement structures appear in red, whereas the more conductive sediments above and below the basalt are plotted in blue. The shallow sediments, the basalt sequence, and the uppermost subbasalt sediments appear to be electric anisotropic; see further discussion in the text. The locations of the Brugdan and Rosebank wells are marked in black.



out within the basalt sequence (Figure 6c), which indicate that the velocity used is too high. However, considering the velocities measured in the well (Figure 9b), we think that the velocities in the basalt sequence must be at least 4900 m/s or higher. We believe that the curved events are due to a mix of the remaining multiple energy, out-of-plane reflections, and aliasing artifacts, because the angle gathers are computed from subsurface offset common-image gathers with a limited aperture. Next, an attempt was made to pick the base of the basalt sequence on the migrated image. However, the subbasalt velocity structure is poorly constrained by the seismic data. The subbasalt reflections in the data set have small amplitudes, and they are affected by noise. Moreover, these events have small reflection angles and very limited moveout due to the overlaying high-velocity basalt sequence as illustrated in Figure 1. Velocity analysis algorithms, such as residual moveout tomography or wave-equation migration velocity analysis, will therefore fail. Instead, we made an attempt to manually estimate the subbasalt velocities by analyzing the angle gathers (e.g., Figure 6c) for several models with varying constant subbasalt velocities, and we found the velocity to be on the order of approximately 4000 m/s (Figure 6a). However, a wide range of subbasalt velocities will produce nearly flat angle gathers due to the small reflection angle and small moveout. It is very hard to improve the velocity estimation further due to the insufficient information on subbasalt velocity structure in the seismic data. Therefore, we need to incorporate additional data, such as CSEM, MT, and well data to further constrain the velocity model.

Resistivity model from electromagnetic data

The CSEM and MT data used as input in this study incorporate measurements from two separate EM surveys: one large EM survey acquired in the autumn of 2012 and an extension toward the northwest acquired in the autumn of 2014. We use only a part of the survey data constituting a 105 km long, regional 2D line. The survey line ranges from the East Faroe High in the northwest over the Corona Basin and the Corona Ridge to the Flett Basin in the

southeast. The Brugdan well (6104/21-1) and the Rosebank well (213/27-1) are situated along this line (Figure 3). The data set includes the measurements from 70 ocean-bottom EM receivers that recorded the time-varying horizontal components of the electric and magnetic fields. The receiver separation was 1.5 km, and the water depth varied between 189 and 1157 m. A horizontal electric dipole source was towed 30 m above the seafloor, emitting a time-varying electric current of 1150 A. A data example is shown in Figure 7.

The CSEM and MT data can be acquired with the same ocean-bottom receivers, but CSEM data were only processed for the time intervals when the electric dipole source was active and towed in proximity to the receivers. For this imaging study, CSEM data for the frequencies 0.2, 0.6, and 1.0 Hz were used (Figure 7a). The MT data were processed from the time intervals when the CSEM source was not active or far from the receiver. MT data in the frequency range 0.6 mHz–0.5 Hz showed a good signal-to-noise ratio and were used for this study (Figure 7b).

We carried out CSEM and MT data inversion using a Gauss-Newton-type joint inversion scheme with a 2.5D finite-element forward modeling operator (Key, 2012). The inversion software uses Occam-type model optimization, which seeks the smoothest possible model that explains the data within the given data uncertainty. The resistivity model was considered to be vertically transversely isotropic (VTI), described by a vertical resistivity R_v and a horizontal resistivity R_h . Anisotropy regularization was applied to stabilize the inverse problem. This regularization penalizes large differences between R_v and R_h . However, anisotropy may develop if the minimization of the data misfit requires it. A uniform subsurface with $R_v = 2 \Omega\text{m}$ and $R_h = 1 \Omega\text{m}$ served as the initial model. The depth to the top-basalt reflector is well-defined by the seismic data, and it was therefore used as a structural constraint. Smoothness regularization was released at this interface, which allows the inversion to introduce a strong resistivity contrast at the location of the top-basalt reflector. The resulting resistivity model (Figure 8) explains the CSEM and MT data well within the data uncertainty with an rms error of 1.09. Examples of observed and synthetic responses are shown in Figure 7. The subbasalt resistivity model is consistent with

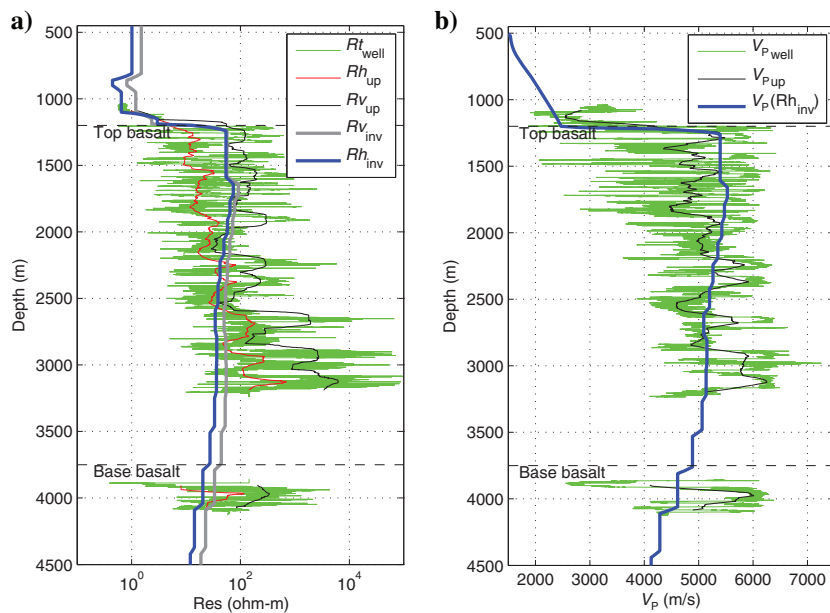


Figure 9. Comparison of the measured well-log data (green line) from the Brugdan well (6101/21-1) with (a) the CSEM and MT joint inversion result (blue and gray line) and (b) the derived velocities. The resistivity well log and the acoustic log were upscaled for better comparison (black and red lines).

our previously published result (Panzner et al., 2014), in which we did not impose a top-basalt structural constraint to the inversion and we only used the data from the 2012 survey. There is good agreement between the inversion result and the reported thickness of the basalt sequence in the two wells at Brugdan and Rosebank. The inversion result is compared with the resistivity data measured in the Brugdan well (Figure 9a), showing good agreement considering the low resolution of the EM data. Hoversten et al. (2013) carry out an EM imaging study using data from the 2012 EM survey and obtain similar results for the southeast part of the resistivity section (Figure 8a). The conductive anomaly northwest of the Brugdan well location (Figure 8a), at a depth greater than 10 km is difficult to explain geologically but is required by the MT data. Also, a totally unconstrained

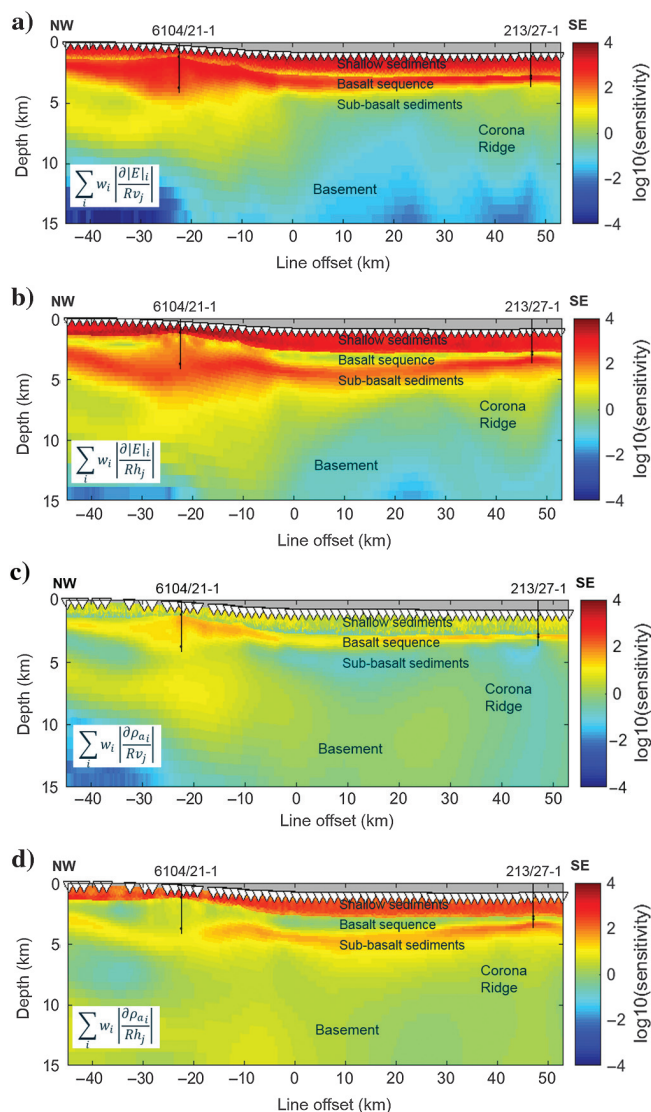


Figure 10. The relative sensitivities for CSEM and MT data are shown for the resulting resistivity model (Figure 8) as the weighted sum of the data sample derivatives with respect to model parameters. (a) The CSEM sensitivities are displayed for the measured electric field amplitudes with respect to changes in the vertical resistivity and (b) in the horizontal resistivity. The MT sensitivities are displayed for the change in apparent resistivity with respect to changes in the (c) vertical resistivity and (d) horizontal resistivity.

MT data inversion recovers a conductive anomaly at this location (not shown).

The VTI model description, having a vertical R_v and a horizontal R_h resistivity component, accommodates a geology composed of thin horizontal layers with strongly varying resistivity. In the following, we use the term “anisotropy” for the ratio between the vertical R_v and the horizontal resistivity R_h . When imaged with low-frequency methods, such as CSEM and MT, the rock properties will be recovered as effectively anisotropic. However, the data sensitivity toward the two resistivity components can vary due to the polarization of the electric field (e.g., Panzner and Sturton, 2010). The inversion result is weakly anisotropic ($R_v/R_h \leq 2$) in the suprabasalt sediments, in the lower section of the basalt sequence, and in the upper section of the subbasalt sediments (Figure 8b). The remaining parts of the resistivity model appear nearly isotropic ($R_v/R_h \sim 1$). Note that the inversion model can explain the observed data to within the measurement accuracy. So, even though our regularization approach will limit anisotropy, the low-anisotropy model we recovered is in agreement with the measured data.

As an illustration of how well the EM data resolve the two resistivity components, we show in Figure 10 the sensitivity for CSEM and MT data. Sensitivity depends on the resistivity model, and we have computed the sensitivity given the inverted model shown in Figure 8. To the first order, the sensitivity plots show us that both resistivity components should be resolved down to the depth of the subbasalt sediments. There are, however, large relative differences between the sensitivity toward R_v and R_h . In particular, the R_v component may be resolved less accurately than can the R_h component below the basalt layer. In this deeper part of the model, the resistivity is recovered as nearly isotropic, and we expect that it was constrained by the anisotropy regularization.

We have shown that it is possible to retrieve structural and quantitative information about the subbasalt geology using CSEM and MT joint inversion. However, this information cannot be directly used to update the velocity model. In the following section, we establish a relationship between resistivity and velocity using logging data from a nearby well.

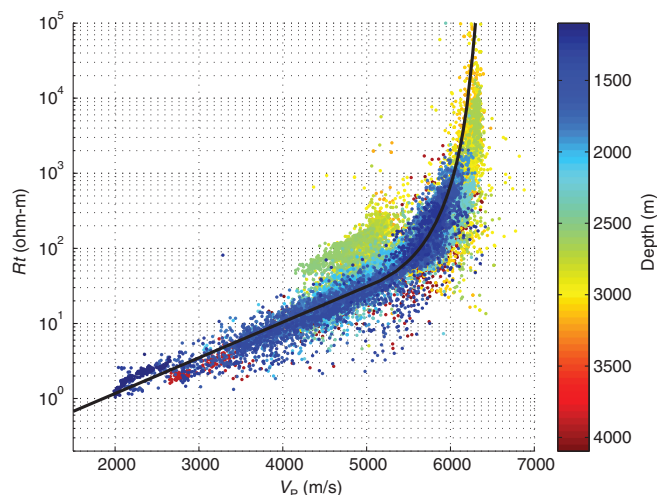


Figure 11. Crossplot of the acoustic-velocity log and resistivity log from the Brugdan well (6104/21-1). The color of the data point indicates the depth in which it was measured. The trend in equation 1 is shown as a black line.

Well-log analysis

We have analyzed the relationship between resistivity and velocity in the logging data from the Brugdan well (Figure 9). There is a clear correlation between the two parameters as seen in Figure 11.

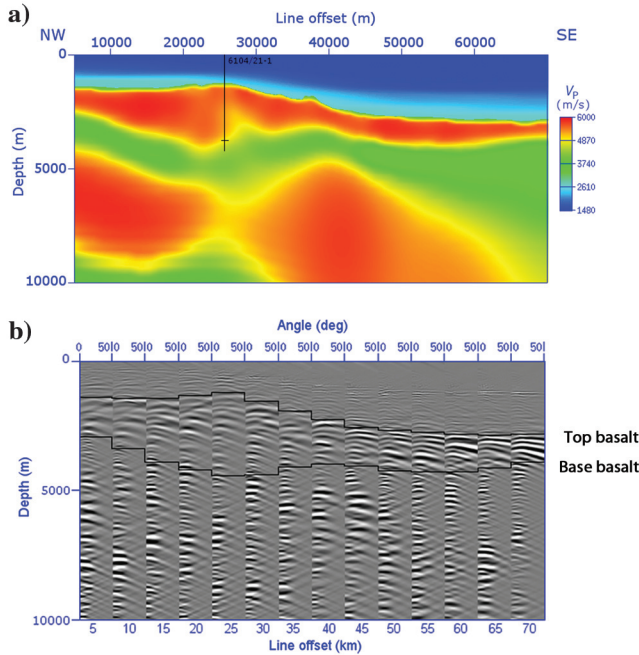


Figure 12. (a) Display of the velocity model with the subbasalt velocity structure updated based on the CSEM and MT joint inversion result from Figure 8. The location of the Brugdan well (6104/21-1) is indicated by a black line. The corresponding subsurface angle common-image gathers are shown in (b) for different positions along the line.

A linear relationship can describe the correlation between the velocity and the logarithm of resistivity for velocities smaller than 5000 m/s. In this velocity-resistivity interval, the correlation is mainly controlled by the porosity, tortuosity, and the pore-fluid resistivity. For velocities larger than 5000 m/s and resistivities greater than 20 Ωm, the correlation approaches an asymptotic behavior of constant velocity for increasing resistivity.

Such an asymptotic relationship between velocity and resistivity can be expected for tight rocks in which the matrix properties and rock composition govern the relevant rock physics. There is no sharp transition between the domain of the two different types of behavior in the crossplot of Figure 11. This is due to the continuously varying lithology. We will describe this statistically as a continuous trend. Curve fitting determines the following empirical relationship for the correlation between resistivity R_t and velocity V_p from the well-log data

$$V_p(R_t) = \begin{cases} 2118 \cdot \log_{10}(R_t) + 1869.5, & \text{if } V_p < 5000 \text{ m/s} \\ \frac{-1239}{\log_{10}(R_t) - 0.701} + 6604, & \text{if } V_p \geq 5000 \text{ m/s} \end{cases} \quad (1)$$

Only a small cluster of data points with the center at $V_p = 5000$ m and $R_t = 100 \Omega\text{m}$ cannot be described by the relationship in equation 1. This cluster represents a few conglomerate layers in the depth interval 2500–3200 m, which follow a different trend. We did not use an exponential function to describe the correlation between high resistivity and velocities, as is done by Heineke et al. (2014), because such an exponential fit cannot explain the correlation for very high resistivities and velocities.

The large dynamic range of resistivity as compared with the range of the velocity, characteristic of this geology, has important implications for the validity of the cross-property relationship. If we consider equation 1 and compute the relative uncertainty in velocity derived from resistivity according to the framework of error

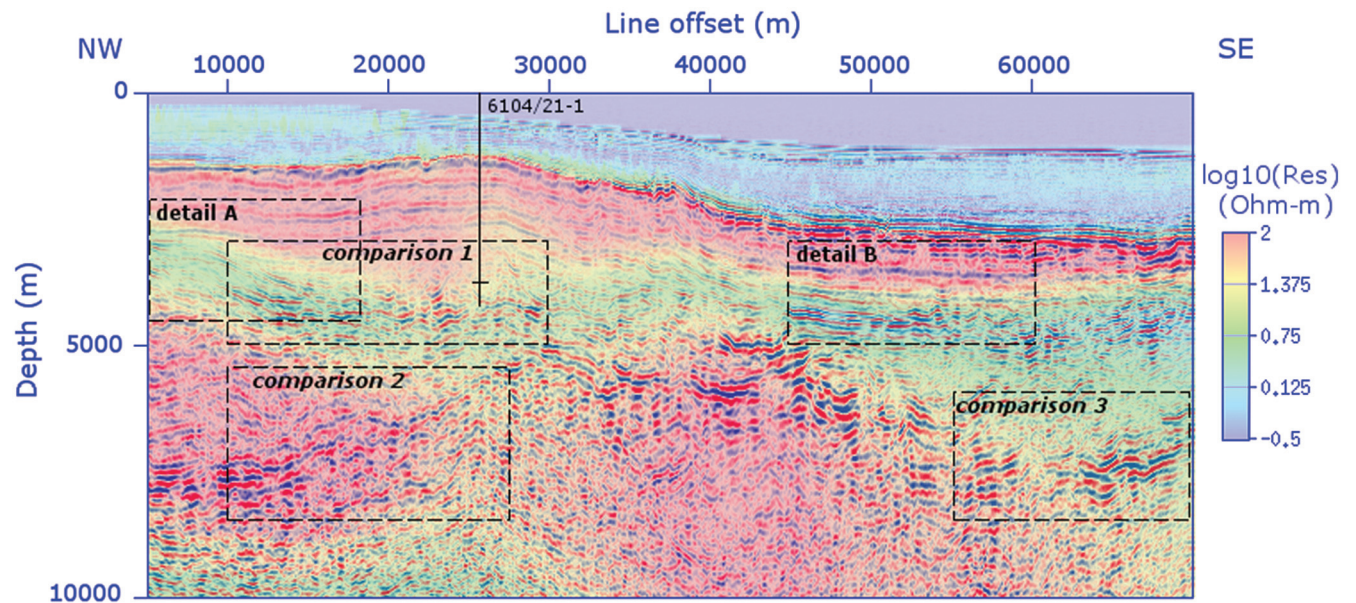


Figure 13. Display of the RTM image for the updated velocity model (Figure 12a), overlaid with the resistivity distribution from CSEM and MT joint inversion. The location of the Brugdan well (6104/21-1) and the reported base of basalt is indicated in black.

propagation $\delta V_P(R_t)/V_P(R_t)$, we find that it is small even when the absolute uncertainty in resistivity δR_t is large at large R_t . The converse is not true, and for the considered geology we find for the relative uncertainty that

$$\frac{\delta V_P(R_t)}{V_P(R_t)} \ll \frac{\delta R_t(V_P)}{R_t(V_P)}. \quad (2)$$

Thus, the cross-property relationship in equation 1 can be used to predict velocity from resistivity $V_P(R_t)$. But the prediction of resistivity from velocity for basalt layers can be expected to give large uncertainty in the resistivity.

Velocity model update based on resistivity information

We will use the empirical relationship $V_P(R_t)$ in equation 1 to convert the resistivity model from CSEM and MT data inversion into a seismic velocity model. The relationship was calibrated on

well-log data that were measured on a much finer spatial scale than the resolution of the seismic data and especially the low-frequency EM data. In principle, the correlation should be determined on up-scaled data to reflect the length scales involved in seismic and EM signal propagation. In particular, the EM propagation scale will be very large due to the low frequencies involved in the measurement. For the present study, we presume that the correlation between up-scaled data can be approximated by the correlation of well-log scale data $\text{corr}\{\hat{V}_P, \hat{R}\} \approx \text{corr}\{V_P, R_t\}$, with \hat{V}_P and \hat{R} being the up-scaled velocity and resistivity. Moorkamp et al. (2013) show that this can be a valid approach, and we may use the relationship in equation 1 to predict the seismic velocities from the resistivities obtained by EM inversion.

The resistivity model is only weakly anisotropic (Figure 8b), which justifies the use of the isotropic resistivity-velocity relationship (equation 1) and the horizontal resistivity model to update the velocity model below the top-basalt interface (Figure 12a). The velocities derived for the suprabasalt sediments are well-constrained by the seismic data and have proven to be valid as discussed earlier.

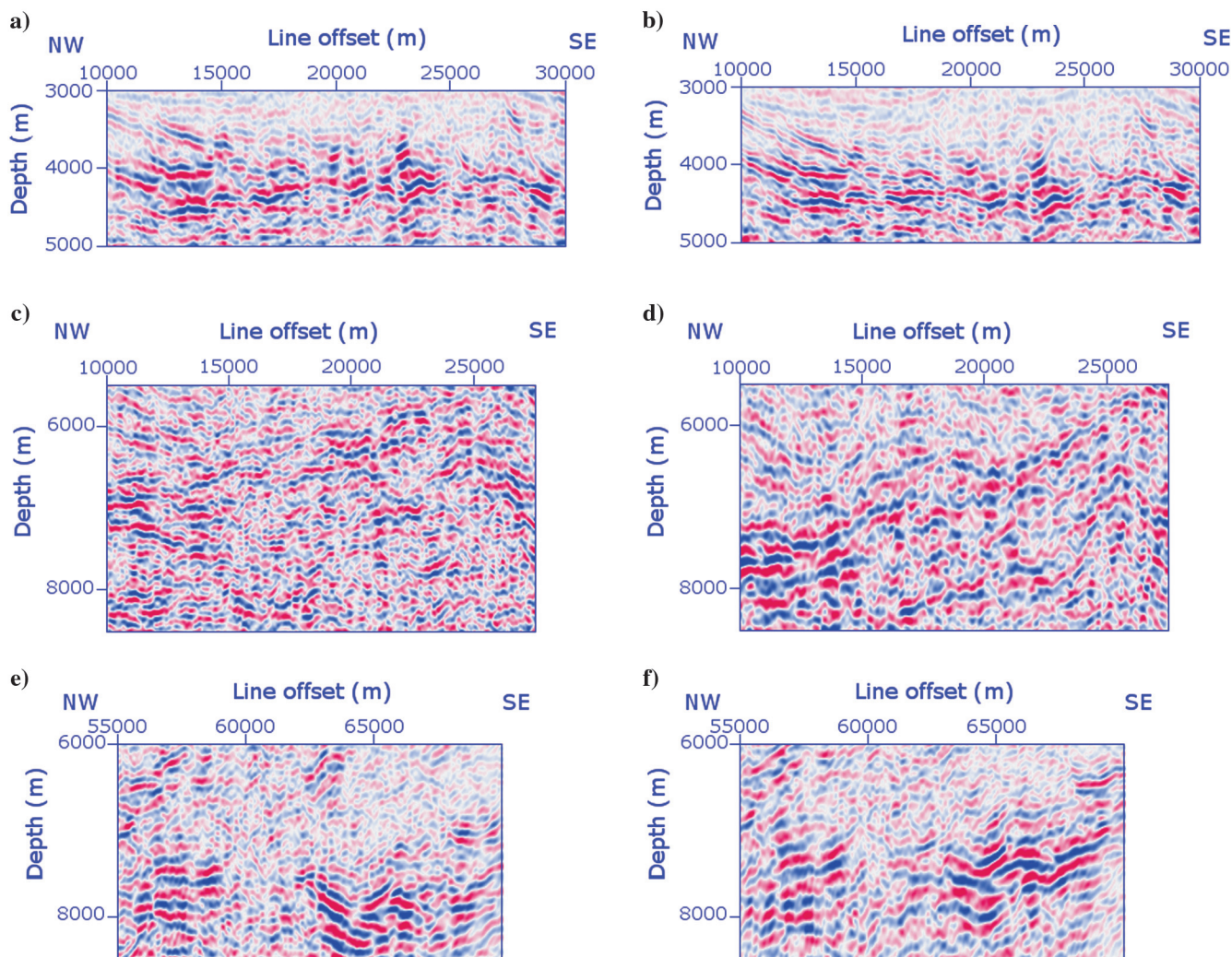


Figure 14. Detailed comparisons of the depth migrated seismic image for the velocity model derived using only seismic data (left) and the CSEM and MT-based velocity model (right) are illustrating the imaging improvements: (a and b) Comparison 1 shows a subbasalt reflector and (c and d) comparisons 2 and (e and f) 3 show the top basement reflector. The locations of the different subsets are marked in Figure 13.

Because the EM line is not exactly collocated with the seismic line, we had to project the model onto the seismic line. This implies that the subsurface structures are presumed to be 2D with a strike direction of north-northeast to south-southwest, which is a reasonable assumption given the a priori information about the geology in the area.

The data were migrated again using the updated model, and the subsurface angle gathers were recomputed (Figure 12b). The angle gathers show a number of flat subbasalt events but only for small angles, which makes it difficult to use these events for validating the velocity model as discussed earlier. Again, there are a number of nonflat events within the basalt sequence. These events do not have a larger curvature than in the angle gathers computed from the constant basalt velocity (Figure 6c) model, which had a significantly lower velocity in the basalt sequence. That makes us confident that these events are not true reflections but a mix of remaining multiple energy, out-of-plane reflections, and aliasing artifacts, as suggested earlier. A comparison of the measured well-log data, the CSEM and MT joint inversion results, and the updated velocity model at the Brugdan well location is shown in Figure 9. The resistivity well log R_l was upscaled using an arithmetic and a harmonic mean for the vertical \hat{R}_v and the horizontal resistivities \hat{R}_h , respectively. An effective vertical velocity \hat{V}_p was computed using the Backus formula (Stovas and Arntsen, 2006). The derived velocity model shows a good correspondence with the upscaled well data (Figure 9b), keeping in mind the low resolution of the EM data. As a consequence, the updated velocity model is also rather smooth.

IMPROVED IMAGING RESULTS

A new RTM was run using the updated velocity model shown in Figure 12a. The resulting migrated image is shown in Figure 13, overlaid with the resistivity distribution from joint CSEM and MT inversion.

The subbasalt reflections in the image are generally more focused, and the base basalt reflector is better defined in parts of the image. A detailed comparison of three selected areas is given in Figure 14. The position, slope, and shape of important reflectors such as the top basement reflector are changed significantly (Figure 14d and 14f).

In addition to improving the velocity model, the resistivity data can enhance the definition of often-unclear subbasalt reflectors by corendering the migrated seismic image and the resistivity model. The independent data types, CSEM & MT, and seismic, give complementary information about the subsurface structures, which enhances the interpretation. For instance, the base of the basalt sequence will be interpreted differently when considering the resistivity image (Figure 15). Furthermore, the quantitative resistivity information can give valuable insight into the lithology and allows us to differentiate between the resistive volcanic layers in the basalt sequence, the more conductive sediments below, and the resistive crystalline basement structures underneath.

DISCUSSION

One challenge with the presented workflow is that the velocity-resistivity relation must be properly calibrated to well data. Such data are typically only available for a very limited depth range and at few lateral positions. This introduces a systematic bias if

the lithology varies significantly from the position of the well. In particular, there is limited penetration below the basalt, so the relationship can be assumed to be less accurate for the subbasalt sediments and the basement rocks.

Another issue with the data sets considered here is that the orientation of the seismic and EM survey lines is not the same. At the southeast end of the seismic line, the maximum distance to the CSEM and MT line is 8.5 km. However, it is known that the subsurface structures in this area are more or less 2D with a strike direction north-northeast to south-southwest, which is nearly perpendicular to the headings of the CSEM and MT and the seismic line, and the effects of increasing line separation toward southeast should be minor.

As indicated in the diagram in Figure 2, the workflow can be applied in an iterative manner. This means that the improved migrated image together with the resistivity image can be used to reinterpret seismic reflectors related to structural boundaries, such as the base basalt reflector or the top basement reflector. The updated structural information can then be used in the subsequent EM inversion. This feedback mechanism is reminiscent of a joint inversion approach. Software that can automatically update the resistivity and velocity models has been devised, and encouraging results have been presented (Medina et al., 2012; Heincke et al., 2014). However, in the workflow presented here, we use conventional processing methods as the building blocks. This has the advantage that it gives greater control, and it allows the consideration of each intermediate step with the possibility to include geophysical knowledge by way of interpretation and parameter adjustments.

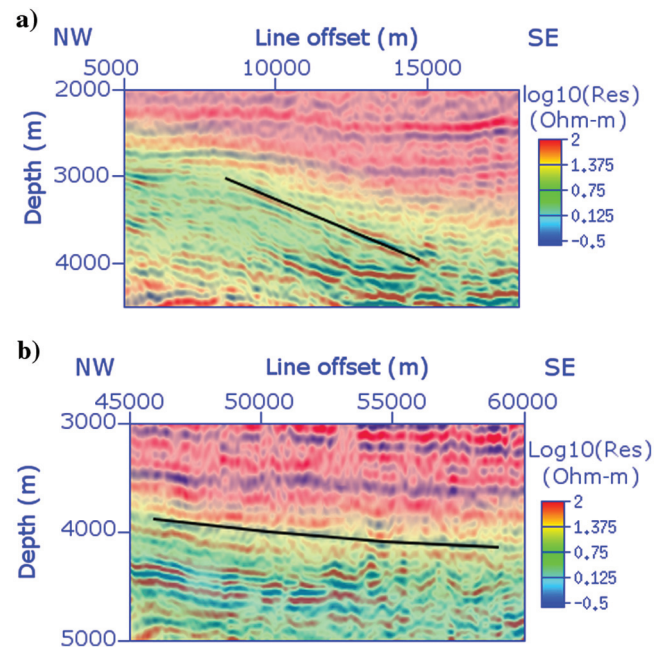


Figure 15. Detailed correlation of the seismic image and the resistivity model. (a) A dipping reflector marked “A” shows good consistency with the base of the resistive basalt sequence. (b) The base of the basalt sequence, marked “B,” is better defined and easier to interpret after migration with the updated velocity model and co-visualization with the resistivity model. The locations of the two subsets are indicated in Figure 13.

CONCLUSIONS

Using a real data set, we have demonstrated that integrated seismic and EM imaging can improve seismic depth migration in a challenging basalt environment. The seismic data have insufficient information about the subbasalt velocity structure, but incorporating complementary information from CSEM and MT surveys allows us to better constrain the velocity model. Moreover, the structural understanding and the interpretation of subbasalt reflectors can be supported by using the resistivity information directly in the interpretation process. For the specific example considered here, we demonstrate significant imaging improvements that can alter the interpretation.

The results presented in this paper were achieved with conventional seismic and EM data processing and imaging techniques. The workflow followed in this study is straightforward to integrate into established depth imaging workflows. An advantage of this sequential approach is that it utilizes the sensitivities of the different data types to different parts of the model. It allows direct control and manipulation of intermediate results to harness other geophysical insight and experience in the process. Therefore, we believe that the methodology described and exemplified in this paper can be of use to a wide range of depth imaging groups, using standard software and processes that are already available.

ACKNOWLEDGMENTS

We wish to thank EMGS for the permission to publish these results. Special thanks go to the Modeling and Seismic Imaging Group at the Institute of Petroleum Technology Department at the Norwegian University of Science and Technology for fruitful discussions and giving us access to their seismic processing and imaging software. We also thank R. Mittel for interesting discussions. J. P. Morten acknowledges support from the Research Council of Norway, and he also thanks the Institute of Geophysics and Planetary Physics at Scripps Institution of Oceanography for graciously hosting him while the manuscript was being finalized. We thank S.-K. Foss, R. Hobbs, and two anonymous reviewers who made comments that helped us to improve our manuscript.

REFERENCES

- Alumbaugh, D., M. Hoversten, J. Stefani, and C. Thacher, 2013, A 3D model study to investigate EM imaging of sub-basalt structures in a deep-water environment: 83rd Annual International Meeting, SEG, Expanded Abstracts, 765–769.
- Chave, A. D., and A. G. Jones, 2012, Introduction to the magnetotelluric method: Cambridge University Press.
- Colombo, D., and M. De Stefano, 2007, Geophysical modeling via simultaneous joint inversion of seismic, gravity, and electromagnetic data: Application to prestack depth imaging: *The Leading Edge*, **26**, 326–331, doi: [10.1190/1.2715057](https://doi.org/10.1190/1.2715057).
- Colombo, D., M. Mantovani, S. Hallinan, and M. Virgilio, 2008, Sub-basalt depth imaging using simultaneous joint inversion of seismic and electromagnetic (MT) data: A CRB field study: 78th Annual International Meeting, SEG, Expanded Abstracts, 2674–2678.
- Colombo, D., G. McNeice, N. Raterman, M. Zinger, D. Rovetta, and E. Sandoval Curiel, 2014, Exploration beyond seismic: The role of electromagnetics and gravity gradiometry in deep water subsalt plays of the red sea: *Interpretation*, **2**, no. 3, SH33–SH53, doi: [10.1190/INT-2013-0149.1](https://doi.org/10.1190/INT-2013-0149.1).
- Eidesmo, T., S. Ellingsrud, L. MacGregor, S. Constable, M. Sinha, S. Johansen, F. Kong, and H. Westerdahl, 2002, Sea bed logging (SBL): A new method for remote and direct identification of hydrocarbon filled layers in deepwater areas: *First Break*, **20**, 144–152, doi: [10.1046/j.1365-2397.2002.00264.x](https://doi.org/10.1046/j.1365-2397.2002.00264.x).
- Fruehn, J., M. M. Fliedner, and R. S. White, 2001, Integrated wide-angle and near-vertical subbasalt study using large-aperture seismic data from the Faeroe-Shetland region: *Geophysics*, **66**, 1340–1348, doi: [10.1190/1.1487079](https://doi.org/10.1190/1.1487079).
- Fruehn, J., R. White, K. Richardson, M. Fliedner, E. Cullen, C. Latkiewicz, W. Kirk, and J. Smallwood, 1998, FLARE — A two-ship experiment designed for sub-basalt imaging: 68th Annual International Meeting, SEG, Expanded Abstracts, 94–97.
- Funck, T., M. S. Andersen, J. Keser Neish, and T. Dahl-Jensen, 2008, A refraction seismic transect from the Faroe islands to the Hatton-Rockall basin: *Journal of Geophysical Research: Solid Earth*, **113**, 1978–2012, doi: [10.1029/2008JB005675](https://doi.org/10.1029/2008JB005675).
- Gallagher, J. W., and P. W. Dromgoole, 2007, Exploring below the basalt, offshore Faroes: A case history of sub-basalt imaging: *Petroleum Geoscience*, **13**, 213–225, doi: [10.1144/1354-079306-711](https://doi.org/10.1144/1354-079306-711).
- Gallardo, L. A., and M. A. Meju, 2007, Joint two-dimensional cross-gradient imaging of magnetotelluric and seismic traveltime data for structural and lithological classification: *Geophysical Journal International*, **169**, 1261–1272, doi: [10.1111/j.1365-246X.2007.03366.x](https://doi.org/10.1111/j.1365-246X.2007.03366.x).
- Heincke, B., M. Jegen, M. Moorkamp, and R. W. Hobbs, 2014, Joint-inversion of magnetotelluric, gravity and seismic data to image sub-basalt sediments offshore the Faroe-Islands: 84th Annual International Meeting, SEG, Expanded Abstracts, 770–775.
- Herredsvela, J., A. Colpaert, S. Foss, A. Nguyen, K. Hokstad, S. Morten, C. Twarz, S. Fanavoll, and F. Mrope, 2012, Feasibility of electromagnetic methods for sub-basalt exploration: 82nd Annual International Meeting, SEG, Expanded Abstracts, 1–5.
- Hoversten, G., D. Myer, K. Key, O. Hermann, R. Hobbet, and D. Alumbaugh, 2013, CSEM and MMT base basalt imaging: 75th Annual International Conference and Exhibition, EAGE, Extended Abstracts, Th-11-10.
- Jegen, M. D., R. W. Hobbs, P. Tarits, and A. Chave, 2009, Joint inversion of marine magnetotelluric and gravity data incorporating seismic constraints: Preliminary results of sub-basalt imaging off the Faroe shelf: *Earth and Planetary Science Letters*, **282**, 47–55, doi: [10.1016/j.epsl.2009.02.018](https://doi.org/10.1016/j.epsl.2009.02.018).
- Key, K., 2012, Marine EM inversion using unstructured grids: A 2D parallel adaptive finite element algorithm: 82nd Annual International Meeting, SEG, Expanded Abstracts, 1–5.
- MacGregor, L., and M. Sinha, 2000, Use of marine controlled-source electromagnetic sounding for sub-basalt exploration: *Geophysical Prospecting*, **48**, 1091–1106, doi: [10.1046/j.1365-2478.2000.00227.x](https://doi.org/10.1046/j.1365-2478.2000.00227.x).
- Medina, E., A. Lovatini, F. G. Andreasi, S. Re, and F. Snyder, 2012, Simultaneous joint inversion of 3D seismic and magnetotelluric data from the walker ridge: *First Break*, **30**, 85–88.
- Moorkamp, M., B. Heincke, M. Jegen, A. Roberts, and R. Hobbs, 2011, A framework for 3-D joint inversion of MT, gravity and seismic refraction data: *Geophysical Journal International*, **184**, 477–493, doi: [10.1111/j.1365-246X.2010.04856.x](https://doi.org/10.1111/j.1365-246X.2010.04856.x).
- Moorkamp, M., A. W. Roberts, M. Jegen, B. Heincke, and R. W. Hobbs, 2013, Verification of velocity-resistivity relationships derived from structural joint inversion with borehole data: *Geophysical Research Letters*, **40**, 3596–3601, doi: [10.1002/grl.50696](https://doi.org/10.1002/grl.50696).
- Morten, J., C. Twarz, V. V. Ricoy-Paramo, and S. Sun, 2013, Improved resolution salt imaging from 3D CSEM anisotropic inversion: 75th Annual International Conference and Exhibition, EAGE, Extended Abstracts, Th-11-12.
- Naif, S., K. Key, S. Constable, and R. L. Evans, 2013, Melt-rich channel observed at the lithosphere-asthenosphere boundary: *Nature*, **495**, 356–359, doi: [10.1038/nature11939](https://doi.org/10.1038/nature11939).
- O'Doherty, R., and N. Anstey, 1971, Reflections on amplitudes: *Geophysical Prospecting*, **19**, 430–458, doi: [10.1111/j.1365-2478.1971.tb00610.x](https://doi.org/10.1111/j.1365-2478.1971.tb00610.x).
- Oldenburg, D. W., 1974, The inversion and interpretation of gravity anomalies: *Geophysics*, **39**, 526–536, doi: [10.1190/1.1440444](https://doi.org/10.1190/1.1440444).
- Panzner, M., and S. Sturton, 2010, Anisotropic sensitivity study for subsalt and subbasalt imaging using CSEM: Presented at the EMGS International Workshop, C PP 01.
- Panzner, M., W. W. Weibull, and J. P. Morten, 2014, Sub-basalt imaging in the Faeroe-Shetland basin using CSEM&MT data to constrain the velocity model: 84th Annual International Meeting, SEG, Expanded Abstracts, 3806–3810.
- Stovas, A., and B. Arntsen, 2006, Vertical propagation of low-frequency waves in finely layered media: *Geophysics*, **71**, no. 3, T87–T94, doi: [10.1190/1.2197488](https://doi.org/10.1190/1.2197488).
- Um, E. S., M. Commer, and G. A. Newman, 2014, A strategy for coupled 3D imaging of large-scale seismic and electromagnetic data sets: Application to subsalt imaging: *Geophysics*, **79**, no. 3, ID1–ID13, doi: [10.1190/geo2013-0053.1](https://doi.org/10.1190/geo2013-0053.1).
- Weibull, W., and B. Arntsen, 2013, Reverse time demigration using the extended imaging condition: 83rd Annual International Meeting, SEG, Expanded Abstracts, 4015–4020.
- White, R. S., J. R. Smallwood, M. M. Fliedner, B. Boslaugh, J. Maresh, and J. Fruehn, 2003, Imaging and regional distribution of basalt flows in the Faeroe-Shetland basin: *Geophysical Prospecting*, **51**, 215–231, doi: [10.1046/j.1365-2478.2003.00364.x](https://doi.org/10.1046/j.1365-2478.2003.00364.x).